Hyperspectral Image Classification via Exploring Spectral–Spatial Information of Saliency Profiles

Qikai Lu, *Member, IEEE*, and Xuan Hu

***Abstract*—Morphological features have shown promising performances for hyperspectral image (HSIs) classification, as they can efficiently extract the multilevel spatial information of HSIs. However, the objects in the scenes are always with different sizes and shapes, making it difficult to excavate spatial information of important structures completely by the existing morphological methods. To address this problem, we propose a novel two-stage framework based on morphology and superpixel. Specifically, we propose self-dual saliency profiles (SPs) based on a saliency measure considering the grayscale contrast within objects and edge information. SPs are hierarchical features that characterize spatial information for salient objects whose saliency index is the significant local maxima. The SPs are constructed based on a two-step algorithm. First, all salient objects of different shapes in the scene are preserved, and the undesired spatial details are discarded by attribute filters based on the saliency measure. Second, the morphological feature is generated based on the organization structure of salient objects in the scene, which provides hierarchical spatial features of the image. Then, the superpixel segmentation is performed on each of the extracted SPs on the basis of the spatial information of salient objects. And, two types of superpixel-based features are extracted from SPs to exploit the information in SPs. The extracted innersuperpixel and intersuperpixel features are fused with spectral information to produce the classification map. The experiments conducted on three HSIs show that, the proposed approach significantly outperforms the other state-of-the-art methods.**

***Index Terms*—Hyperspectral images (HSIs), mathematical morphology, morphological saliency profiles (SPs), spatial–spectral classification, superpixel.**

I. Introduction

THE hyperspectral sensors can collect and process hundreds of adjacent narrow-band spectral information from the visible spectrum to the infrared spectrum. Thanks to the detailed spectral information, different kinds of objects on the surface of the earth can be easily distinguished [1]. Hence, hyperspectral images (HSIs) have been widely applied in different areas, such as geological science [2], military applications [3], precision agriculture [4], and ecological science [5]–[7]. Among these tasks, supervised classification is used to distinguish the different materials of interest, which plays a vital role in HSIs analysis.

With the improvement of the spatial resolution of HSIs, more structural and contextual information can be obtained from images [8]. Meanwhile, classification approaches using both spectral and spatial information have attracted increasing attention. Researchers have proposed different methods to model the contextual information from HSIs, such as Markov random fields [9], 3-D Gabor feature extraction [10], edge-preserving filtering [11], sparse representation model [12], hybrid-graph learning method [13], [14], morphological feature-based method [15], [16], and deep learning-based method [17]–[19]. Among these methods, morphological features show satisfactory classification performance.

Morphological profiles (MPs) [20] were first introduced for the segmentation and classification of high-resolution remote sensing images. MPs are generated by repeatedly using morphological filters by reconstruction on the basis of a sequence of structuring elements (SE) with different sizes. These morphological transformations remove trivial details and preserve regions containing useful spatial information. For instance, darker and brighter regions that are smaller than SE are removed in the image by closing and opening with reconstruction, respectively. However, the regions that are larger than the SE are preserved by the morphological transformation. Therefore, the spatial information of the area defined by SE can be extracted by performing the morphological transformation. Then, extended MPs (EMPs) are proposed to extract morphological profiles from HSIs [21]. First, the dimensionality reduction (DR) method is applied to reduce the dimension of features while preserving the important information of the image, such as principal component analysis (PCA) [22], local geometric structure Fisher analysis (LGSFA) [23], and hypergraph methods [24]. Then, the morphological transformations are performed on the extracted components. Specifically, MPs were used to analyze areas damaged by the earthquakes in Bam on a high-resolution image captured by Quickbird [25]. MPs were investigated in [26] by interpreting MP as a fuzzy measurement to characterize the size and contrast of the structures, and then the decision is made based on the possibility distribution modeled by using the expert's knowledge. The derivative of the morphological profile (DMP) that measures the slope of two successive opening-closing morphological profiles as the structural feature was utilized to generate the candidate segment in the hierarchical segmentation [27]. A banded-PSO optimization approach based on fractional-order Darwinian particle swarm optimization [28]

Manuscript received March 28, 2020; revised May 18, 2020; accepted June 2, 2020. Date of publication June 17, 2020; date of current version June 25, 2020. This work was supported in part by the National Key Research and Development Program of China under Grant 2019YFB2102902 and in part by the Open Fund of Key Laboratory of Urban Land Resources Monitoring and Simulation, MNR, under Grant KF-2019-04-006. *(Corresponding author: Qikai Lu.)*

Qikai Lu is with the Faculty of Recourses and Environmental Science, Hubei University, Wuhan 430062, China (e-mail: qikai_lu@hotmail.com).

Xuan Hu is with the State Key Laboratory of Information Engineering in Surveying, Mapping and Remote Sensing, Wuhan University, Wuhan 430079, China (e-mail: xuanhu@whu.edu.cn).

Digital Object Identifier 10.1109/JSTARS.2020.3003053

was proposed in [29], which can select the optimal bands of MPs for the classification task. It can be found that the methods based on MPs showed satisfactory classification results since the morphological feature is adept at characterizing multiscale structural information of objects in the scene. However, the shape of SE is fixed in the traditional morphological filter, which makes it difficult for MPs to adaptively model objects of different shapes. On the other hand, SEs only characterize the scale or shape information of the objects, which are inappropriate to extract gray-level information of the regions [30].

In recent years, morphological attribute profiles (APs) were proposed to characterize the objects with different kinds of attributes related to geometrical properties and gray-scale information, rather than the scale of the regions [31]. APs are constructed by continuously performing morphological attribute filters (AFs) with different thresholds, which form a multiscale representation of the spatial information in the image. AFs are connected operators that are region-based filters since they only merge the connected components under certain conditions [32]. The connected components are the regions where the grayscale of pixels is constant. The extensive or antiextensive attribute filters are performed on a min-tree and max-tree, respectively, which are hierarchical tree representations composed of connected components. Then, the nodes which are ineligible for certain conditions are removed. Finally, the pruned tree is translated as an image that is filtered output [33]. The advantage of AFs is that the edges in the image are preserved during the filtering process since these filters only merge connected components that exist in the input image [34]. The most used attributes for AFs are area, volume, standard deviation, convex-hull area, and the moment of inertia. These attributes can describe objects in the image not only from the perspective of scale but also from the perspective of other measures such as geometrical, grayscale, and textural. As a generalization of the APs, extended multiattribute profiles (EMAPs) are developed to extract morphological features from HSIs by computing APs on the first few components of HSIs [35]. A detailed review of the morphological attribute profile and its associated methods can be found in [36]. Besides, extinction profiles (EPs) are proposed to improve the classification accuracy and simplification ability of APs [16]. EPs are extrema-oriented features, which are constructed by performing a set of extinction filters (EFs) [37]. EFs are connected filters based on extinction value that measures the persistence of extrema [38]. Hence, EFs can preserve the most stable extrema regions and discard other unimportant regions, which make EPs have better simplification capability for recognition than APs. Also, EPs have been investigated for fusing with spectral features to perform classification via deep CNN [39] and a low-rank technique [40].

However, the aforementioned methods cannot completely characterize structural information of the image, since objects in the scene are always with complex variations in shapes and sizes. To capture the complex spatial information of objects, we propose a novel classification approach to extract multilevel spatial information of salient objects from HSIs with a new self-dual morphological feature called morphological saliency profiles (SPs). First, an attribute deduced from the energy function for image segmentation is adopted to compute the saliency index of the node on the tree of shapes (ToS) [41]. ToS is a representation of an image that organizes the connected components whose holes are filled in using a hierarchical tree structure. Then, salient shapes can be selected by a nonincreasing filter based on the attribute. Subsequently, SPs are constructed by repeatedly filtering all leaf nodes of ToS. To exploit the abundant spatial information of SPs, we use the simple linear iterative clustering (SLIC) method to cluster homogeneous pixels of each SP into the superpixels. Subsequently, the innersuperpixel and intersuperpixel features of the SPs are extracted by performing the mean filter and the weighted average filter on superpixels. Finally, multiple kernel learning method is employed to fuse the original spectral feature and the innersuperpixel and intersuperpixel features of the SPs.

The contributions of this article are listed as follows.

1) We propose novel self-dual morphological saliency profiles on the basis of the saliency index of the node on ToS, which preserves the critical structures for objects and discards less important details of the local context.
2) We develop an adaptive feature construction method that generates morphological features based on the organization structure of salient objects in the scene. This method can provide a complete and continuous characterization of spatial information at different scales.
3) We extract the innersuperpixel and intersuperpixel features of SPs to represent the spatial information of HSIs. And, a method that can adaptively determine the number of superpixels in each SP is developed to generate the superpixel segmentation maps.

The rest of the article is organized as follows. The proposed method is described in Section II, including the construction of saliency profiles, the innersuperpixel and intersuperpixel feature extraction based on superpixel segmentation, and image classification using multiple kernel learning (MKL). Section III presents experiments conducted on three real datasets and analyzes the experimental results. Section IV concludes the article.

II. Proposed Method

As shown in Fig. 1, the proposed classification method includes four steps. First, morphological SPs are extracted from the principal components that contain 99% information of HSIs. The second step is shapes-adaptive superpixel maps generation, which performs SLIC method on each SP feature according to the contextual information of SP. Subsequently, the innersuperpixel and intersuperpixel features are computed by applying the mean filter and weighted average filter on superpixels. Finally, the MKL method is adopted to integrate the original spectral feature and innersuperpixel and intersuperpixel features.

A. Saliency Profiles Extraction

The self-dual morphological transformation relies on the ToS, which can be regarded as hierarchical representations of the image. ToS is constructed by merging two simple tree representations (the max-tree and the min-tree) into a single tree. Let $f : \Omega \rightarrow (E, \leq)$ denote a discrete grey image, where

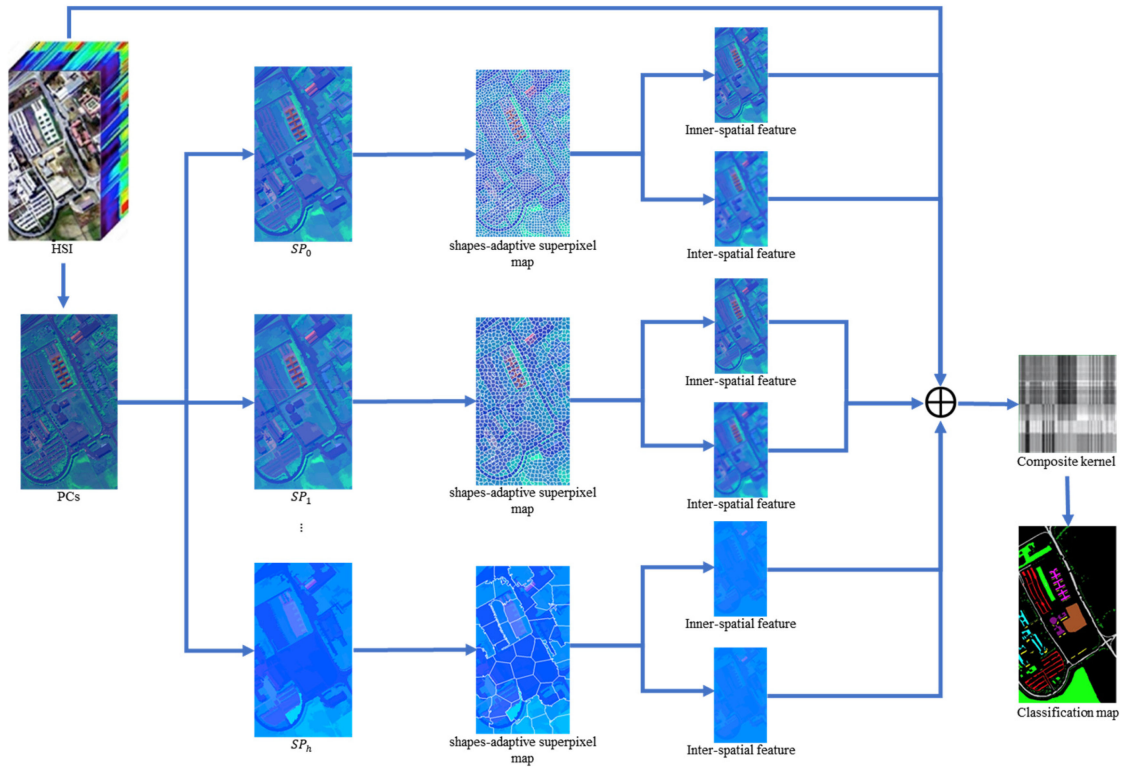

Fig. 1. Flowchart of the proposed framework.

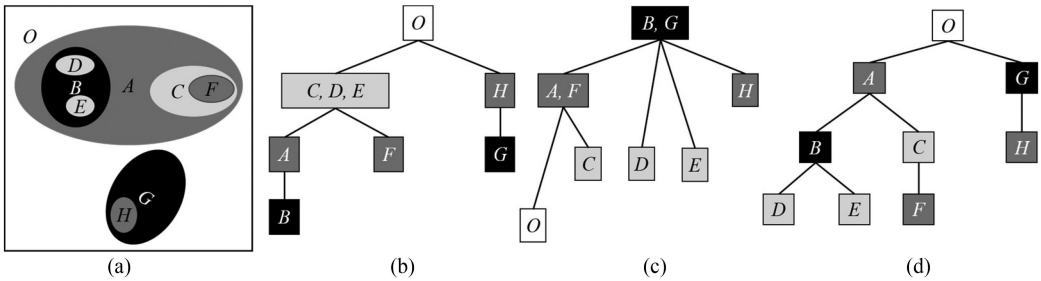

Fig. 2. (a) Image f. (b) Min-Tree. (c) Max-Tree. (d) Tree of shapes.

Ω is the domain of the image f, and E is an ordered set of grayscales. For any given threshold of grayscale $\lambda \in E$, two binary images $\chi_\lambda(f) = \{p \in \Omega | f(p) \geq \lambda\}$ and $\chi^\lambda(f) = \{p \in \Omega | f(p) \leq \lambda\}$ can be obtained by thresholding the image. These two binary images are called upper-level sets and lower level sets. The nodes of the max- and min-tree are, respectively, the connected components of χ_λ and χ^λ, which are defined as $CC(\chi_\lambda)$ and $CC(\chi^\lambda)$. A set of $CC(\chi)$ can be obtained with multilevel thresholding of the image. Thus, these connected components as nodes are organized into a tree structure by the inclusion relation between the connected components. As illustrated in Fig. 2, there is an original image which consists of eight flat zones with four gray-level values. The leaf nodes of the max-tree and the min-tree correspond to the regional maxima and the regional minima, respectively. However, the minima and maxima regions cannot be processed at the same time. ToS (or inclusion tree) can be regarded as a combination of min- and max-tree [46], which is a self-dual data structure and allows filter the dark and bright regions simultaneously. The node of the ToS defined by $sat(CC(\chi))$ is the saturation of the connected component, which are composed of $CC(\chi)$ and the holes of $CC(\chi)$. Since a total relation has been defined, any two nodes of the ToS are either disjoint or nested. Therefore, ToS is constructed according to the inclusion relation between the shapes [see Fig. 2(d)]. The leaves of ToS correspond to the extrema regions, which means that the dark and bright structures can be simplified simultaneously.

The generation of SPs is based on an attribute $\mathcal{A}_\nu$ deduced from regularization parameter ν of the piecewise-constant Mumford–Shah function. The attribute $\mathcal{A}_\nu$ characterizes the importance of shape, and the regularization parameter ν is set to a large value to delete this shape during the minimization of the energy function. The piecewise-constant Mumford–Shah function [43] is a simplified version of the Mumford–Shah model proposed by Mumford and Shah [44], which is based on energy minimization. Let a pair $(\partial R, \tilde{f})$ denote a partition map of the

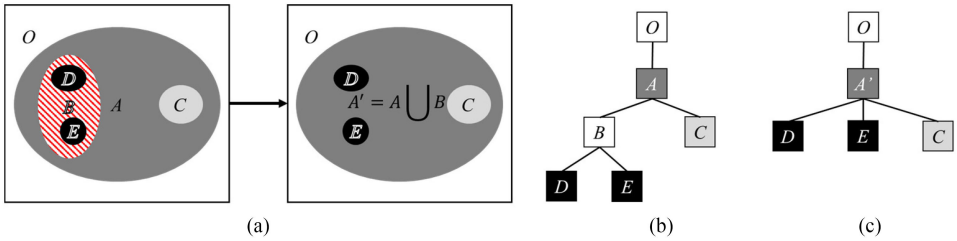

Fig. 3. (a) Example of removing the shape B and update the parenthood relationship. (b) ToS before removing B. (c) ToS after removing B.

input image $f : \Omega \to \mathbb{R}$, where $\tilde{f}$ is the average value of each region $\Omega \backslash \partial R$, and ∂R is the set of pixels belong to the boundaries of regions. A partition map of an image f is computed by the function which is given by

$$E(f, \partial R) = \iint_{\{R\}} (\widetilde{f}_i - f)^2 dxdy + \nu |\partial\{R\}| \tag{1}$$

where $|\partial\{R\}|$ is the total number of pixels belong to the edges $\partial\{R\}$, and the regularization parameter ν is a positive number that controls the degree of simplification. When the regularization parameter ν is lower, the partition map is finer.

For a given ν, whether a shape τ can be removed is determined by the energy function ΔE_τ in (2)

$$\Delta E_\tau = \frac{S^2(f, R_\tau)}{|R_\tau|} + \frac{S^2\left(f, R_{\tau_p}\right)}{\left|R_{\tau_p}\right|} - \frac{S^2\left(f, R'_{\tau_p}\right)}{\left|R'_{\tau_p}\right|} - \nu\,|\partial\tau| \tag{2}$$

where τ_p is the parent node of τ, and $S(f, R_\tau)$ is the sum value of pixel belonging to R_τ.

Assume that ν_{min} satisfies $\Delta E_\tau = \frac{S^2(f,R_\tau)}{|R_\tau|} + \frac{S^2(f,R_{\tau_p})}{|R_{\tau_p}|} - \frac{S^2(f,R'_{\tau_p})}{|R'_{\tau_p}|} - \nu_{min}|\partial\tau| = 0$. When ν is smaller than ν_{min}, the sign of ΔE_τ will be positive, which means this shape should be preserved. The function $E(f, \partial R)$ decrease as the regularization parameter ν increases. Hence, ν_{min} is the critical value that determines whether a shape can be deleted. Let attribute $\mathcal{A}_\nu(\tau)$ denote the critical value of the shape τ, which is defined as

$$\mathcal{A}_\nu(\tau) = \left(\frac{S^2(f, R_\tau)}{|R_\tau|} + \frac{S^2\left(f, R_{\tau_p}\right)}{\left|R_{\tau_p}\right|} - \frac{S^2\left(f, R'_{\tau_p}\right)}{\left|R'_{\tau_p}\right|}\right) / |\partial\tau|\,. \tag{3}$$

To compute $\mathcal{A}_\nu$ of each shape τ, all nodes of the ToS are sorted in ascending order of the average values of the gradient's magnitude along the edge of the shape $\mathcal{A}_\nabla$. As Fig. 3 shows, the attribute $\mathcal{A}_\nu(B)$ of node B is computed according to (3). Subsequently, the underlying node B is removed, and the parenthood relationship of its parent node and child nodes is updated. In this example, the removal of B implies its child nodes D and E become the child of node A. Besides, the pixels that belonged to B are incorporated into its parent node A. Then, the removability of its parent node and child nodes will be changed since the local relationship between nodes have altered as the node B was removed.

This attribute function $\mathcal{A}_\nu$ measures the importance of the shapes. The data fidelity term $\iint_{\{R\}} (\widetilde{f}_i - f)^2 dxdy$ tends to remove low contrast details, and the regularization term $|\partial\{R\}|$ tends to suppress the shapes with complex boundaries. In practice, the meaningful objects in remote sensing images usually have smooth and high contrast edges. Thus, the attribute function $\mathcal{A}_\nu$ measures the saliency of shapes in accordance with homogeneity and boundaries of regions. An example of the attributes $\mathcal{A}_\nabla$ and $\mathcal{A}_\nu$ computed on the first principal component extracted from the hyperspectral data is illustrated in Fig. 4. By observing the curve of attribute value from the leaf (left start point of the curve) to the root node of the ToS (right finishing point of the curve), it can be found that the meaningful objects such as building and playground correspond to the significant local maxima on the curve of $\mathcal{A}_\nu$. The first significant local maxima corresponding to the building can be regarded as the foreground, and the second one can be regarded as the background of this building. The information at different scales is complementary to each other so that multiscale information can enhance the classification performance. This example also shows that the average value of the gradient's magnitude $\mathcal{A}_\nabla$ roughly reflects the saliency of the shapes, which provides a rational sequence for computing the value of $\mathcal{A}_\nu$.

To retain the salient shapes, we predefine a scalar h_ν to select the shapes corresponding to the significant local maxima on the curve of $\mathcal{A}_\nu$. If $\mathcal{A}_\nu(\tau) - \mathcal{A}_\nu(\tau_p) \geq h_\nu$ and $\mathcal{A}_\nu(\tau) - \mathcal{A}_\nu(\tau_c) \geq h_\nu$ for all $\tau_c \in \mathrm{children}(\tau)$, the shape τ can be regarded as a salient shape. Otherwise, the shape τ is regarded as unimportant shape. First, a new tree $\mathcal{T}_0$ is set as $\mathcal{T}_0 = \mathcal{T}$. Then, SP_0 is reconstructed from the tree $\mathcal{T}_0$ whose all unimportant shapes are removed from $\mathcal{T}_0$. Let us define $LF(\mathcal{T})$ represents a self-dual operator of removing all leaf nodes of tree $\mathcal{T}$. Specifically, SP_i is reconstructed from the tree $\mathcal{T}_i = LF(\mathcal{T}_{i-1})$ where i varies from 1 to $h-1$ and h is the height of ToS $\mathcal{T}_0$. The complete SPs are defined by

$$SP = \{RC(\mathcal{T}_0), \ldots, RC(LF(\mathcal{T}_{i-1})), \ldots, RC(LF(\mathcal{T}_{h-2}))\} \tag{4}$$

where $RC(\mathcal{T})$ represents the reconstruction operator that reconstructs an image from a tree. For the hyperspectral data, SPs are computed on the first c PCs that should contain at least 99% of the total variance of the original HSIs.

B. Construction of Shapes-Adaptive Superpixels

In this research, superpixel segmentation is adopted to exploit the spatial information within SPs. As a well-known superpixel segmentation method, SLIC is employed owing to its satisfactory performance in boundary adherence and speed [45]. The required parameter of this method is the number of initial cluster

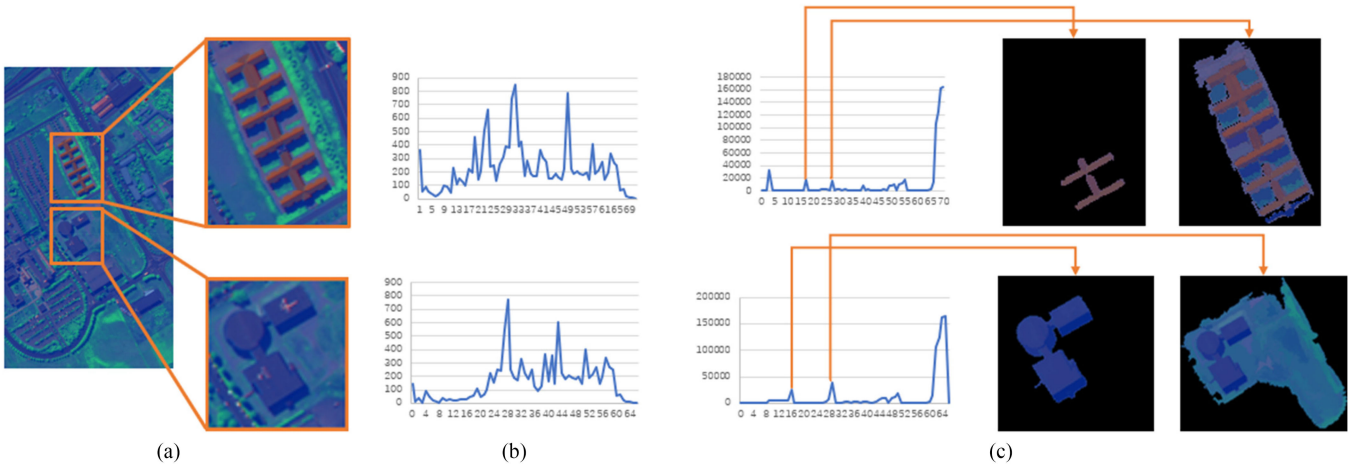

Fig. 4. Example of the $\mathcal{A}_\nu$ of a branch on the HSIs image. (a) University of Pavia image. (b) Curve of $\mathcal{A}_\nabla$ of a branch of the ToS. (c) Curve of $\mathcal{A}_\nu$ and two salient shapes corresponding to two remarkable local maxima value on the curve of $\mathcal{A}_\nu$.

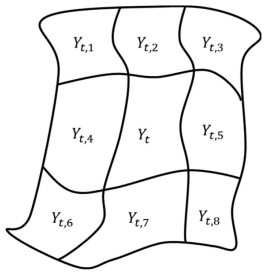

Fig. 5. Example of superpixel Y_t and its adjacent superpixels $Y_{t,1}, \ldots, Y_{t,8}$.

centers k, which is approximately equal to the desired amount of superpixels. How to choose the optimal number of superpixels is a critical problem. At present, most methods [46], [47] choose the number of initial clusters manually, which is challenging to cope with complex image scenes and always time-consuming. In our framework, an adaptive method is adopted to set k automatically according to the number of shapes, as the number of shapes is related to the complexity of the image scene. As shown in Fig. 1, the shapes-adaptive superpixel map is computed on each SP. The number of shapes of ToS can reflect the complexity of the image. For each morphological feature SP_i reconstructed from the tree $\mathcal{T}_i$, the number of superpixels k_i is calculated as follows:

$$k_i = k_0 \times \frac{S_i}{S_0} \tag{5}$$

where k_0 is the number of superpixels for the first feature SP_0, and S_i is the number of shapes of $\mathcal{T}_i$. The parameter k_0 is set according to the size of the image. Then, the number of superpixels k_i for different morphological features SP_i can automatically adjust with the ratio between S_i and S_0.

C. Innersuperpixel and Intersuperpixel Features Extraction

In Fig. 5, a superpixel is composited of a set of adjacent pixels defined by y_t^m, $m = 1, 2, \ldots, M$, where M is the total number of pixels in the superpixel. For each superpixel, the innersuperpixel and intersuperpixel features of the SPs can be acquired by performing the mean filter and the weighted mean filter.

Mean SPs Feature SP^{mean}: The innersuperpixel feature within each superpixel is computed by performing a mean filter on the superpixel. Let $\overline{y_t}$ denotes the average value of all pixels belonging to one superpixel (y_t^m, $m = 1, 2, \ldots, M$). For each superpixel in a SP, the average value is computed and assigned to the pixels belonging to it.

Weighted Mean SPs Feature SP^{weight}: Since the adjacent regions always share the relevant spatial information, the weighted mean method is performed on the adjacent superpixels (i.e.,$Y_{t,n}$, $n = 1, 2, \ldots, N$) of the superpixel Y_t, where N is the number of its adjacent superpixels. An example of superpixel Y_t and its adjacent superpixels are represented in Fig. 5. The intersuperpixel feature is obtained by performing a weighted mean filter on the basis of the adjacent superpixels, which are defined as follows:

$$y_t^{\text{weight}} = \sum_{n=1}^{N} w_{t,n} \times \overline{y_{t,n}} \tag{6}$$

where $w_{t,n} = \frac{\exp(-(\overline{y_t}-\overline{y_{t,n}})^2/s)}{\sum_{n=1}^{N}\exp(-(\overline{y_t}-\overline{y_{t,n}})^2/s)}$ is the weight of the surrounding adjacent superpixel, and s is a predefined scalar, and $\overline{y_{t,n}}$ is the average value of all pixels belonging to the adjacent superpixels $Y_{t,n}$. The larger the dissimilarity between Y_t and $Y_{t,n}$, the lower the weight $w_{t,n}$. Thus, the intersuperpixel feature can capture the information of the neighborhood of the superpixels.

D. Classification by MKL Algorithm

In our work, the multiple kernel learning (MKL) method is adopted to integrate the spectral and spatial features, since it can weigh the features adaptively according to their importance for classification. The basic idea of the multiple kernel learning is to determine the base kernels and the corresponding weights. By optimizing the weight of each basis kernel, the

TABLE I
NUMBERS OF SAMPLES IN DIFFERENT CLASSES IN THE THREE TEST IMAGES

Indian Pines			University of Pavia			Pavia Center		
Class	Name	Number	**Class**	Name	Number	**Class**	Name	Number
1	Corn-notill	1428	**1**	Asphalt	6631	**1**	Water	824
2	Corn-mintill	830	**2**	Meadows	18649	**2**	Trees	820
3	Grass-pasture	483	**3**	Gravel	2099	**3**	Asphalt	816
4	Grass-trees	730	**4**	Trees	3064	**4**	Bricks	808
5	Hay-windrowed	478	**5**	Sheets	1345	**5**	Bitumen	808
6	Soybean-notill	972	**6**	Bare Soil	5029	**6**	Tiles	1260
7	Soybean-mintill	2455	**7**	Bitumen	1330	**7**	Shadows	476
8	Soybean-clean	593	**8**	Bricks	3682	**8**	Meadows	824
9	Woods	1265	**9**	Shadows	947	**9**	Bare Soil	820
10	Bldg-Grass-Trees	386						
Total		9620	**Total**		42776	**Total**		7456

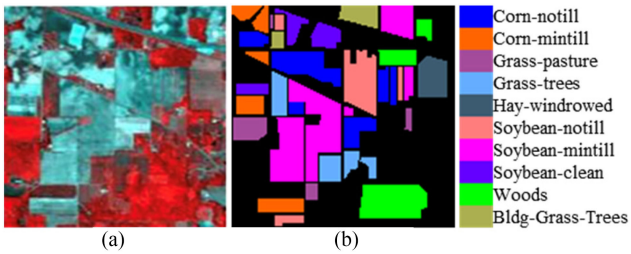

Fig. 6. (a) False-color image of Indian Pines. (b) Its reference data.

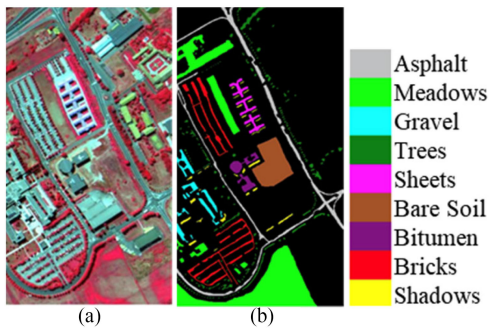

Fig. 7. (a) False-color image of the University of Pavia. (b) Its reference data.

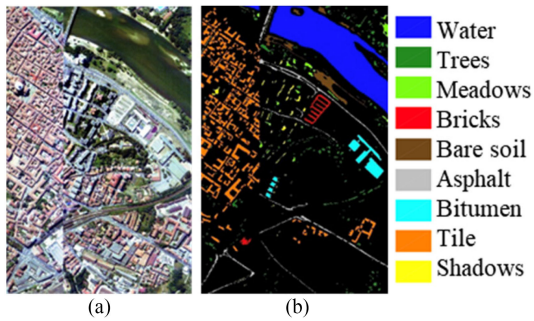

Fig. 8. (a) False-color image of Pavia Center. (b) Its reference data.

useful information inherited in the different features can be better exploited for image classification [48], [49]. Specifically, three RBF kernels are employed as the base kernels of MKL to model the discriminative information of three different features, which is expressed as follows:

$$K^{\text{spec}}\left(y_i^{\text{spec}}, y_j^{\text{spec}}\right) = \exp\left(-\left\|y_i^{\text{spec}} - y_j^{\text{spec}}\right\|^2 / 2\sigma^2\right) \tag{7}$$

$$K^{\text{mean}}\left(y_i^{\text{mean}}, y_j^{\text{mean}}\right) = \exp\left(-\left\|y_i^{\text{mean}} - y_j^{\text{mean}}\right\|^2 / 2\sigma^2\right) \tag{8}$$

$$K^{\text{weight}}\left(y_i^{\text{weight}}, y_j^{\text{weight}}\right) = \exp\left(-\left\|y_i^{\text{weight}} - y_j^{\text{weight}}\right\|^2 / 2\sigma^2\right) \tag{9}$$

where y^{spec}, y^{mean}, and y^{weight} are the spectral feature, the mean SPs feature, and the weighted mean SP s feature, respectively. Then, the composite kernel is obtained by combining the above three kernels through the weighted average method as follows:

$$\begin{aligned} K^{\text{comp}}\left(y_i, y_j\right) = {} & \mu^{\text{spec}} K^{\text{spec}}\left(y_i^{\text{spec}}, y_j^{\text{spec}}\right) \\ & + \mu^{\text{mean}} K^{\text{mean}}\left(y_i^{\text{mean}}, y_j^{\text{mean}}\right) \\ & + \mu^{\text{weight}} K^{\text{weight}}\left(y_i^{\text{weight}}, y_j^{\text{weight}}\right) \end{aligned} \tag{10}$$

where μ^{spec}, μ^{mean}, and μ^{weight} are the weights of three base kernels, respectively, and $\mu^{\text{spec}} + \mu^{\text{mean}} + \mu^{\text{weight}} = 1$. The weighted composite kernel $K^{\text{comp}}\left(y_i, y_j\right)$ is used to replace the single kernel in SVM to generate the classification map.

III. EXPERIMENT STUDY

A. Data Description

1) *Indian Pines:* The Indian Pines data was acquired by the Airborne Visible/Infrared Imaging Spectrometer (AVIRIS) sensor. This sensor provides 224 spectral bands, and the wavelength of the spectrum ranges from 0.4 to 2.5 μm. In this data, the number of spectral channels is reduced to 200 by removing the water absorption bands. This image contains 145 $\times$ 145 pixels, which was taken in the Indian Pines test site in northwestern Indiana. The false-color image and the corresponding ground truth map of the Indian Pines dataset are shown in Fig. 6.

TABLE II
CLASSIFICATION RESULTS ACHIEVED BY DEFERENT METHODS ON THE INDIAN PINES IMAGE

	SVM	EMP	EMAP	EEP	ESP	SC-MK	SF-SP-SVM	SF-SP-MK
Dimensions	200	425	425	750	330	600	860	860
Corn-notill	66.99	70.29	76.79	79.30	92.54	81.00	93.95	**97.26**
Corn-mintill	67.59	70.92	78.60	79.28	94.88	87.78	91.36	**98.10**
Grass-pasture	91.48	90.81	91.34	92.24	97.71	95.61	97.83	**98.31**
Grass-trees	93.71	94.81	96.65	97.40	99.94	97.32	99.38	**99.76**
Hay-windrowed	99.44	99.39	99.65	99.51	100.00	99.98	99.44	**100.00**
Soybean-notill	74.32	69.92	82.66	84.39	94.08	85.80	89.34	**95.93**
Soybean-mintill	55.89	60.64	72.67	74.02	91.86	77.09	91.77	**96.07**
Soybean-clean	72.69	67.66	74.99	79.96	93.08	88.03	93.96	**98.01**
Woods	84.32	85.88	92.91	93.79	99.10	94.04	98.30	**99.83**
Bldg-Grass-Trees	73.27	79.58	92.77	94.88	98.87	94.67	98.36	**99.55**
OA	72.41	74.20	82.33	83.88	95.00	86.50	94.28	**97.72**
AA	77.97	78.99	85.90	87.48	96.20	90.13	95.37	**98.28**
K	68.38	70.40	79.63	81.42	94.19	84.40	93.34	**97.34**

TABLE III
CLASSIFICATION RESULTS ACHIEVED BY DEFERENT METHODS ON THE UNIVERSITY OF PAVIA IMAGE

	SVM	EMP	EMAP	EEP	ESP	SC-MK	SF-SP-SVM	SF-SP-MK
Dimensions	103	51	51	126	81	309	265	265
Asphalt	93.76	98.17	93.46	94.48	97.42	95.37	97.97	**99.56**
Meadows	94.48	98.47	90.88	95.79	98.24	95.62	99.04	**99.59**
Gravel	67.72	73.85	89.47	97.40	98.35	97.76	99.13	**99.32**
Trees	81.87	96.86	97.07	**98.79**	92.78	96.34	98.33	97.02
Sheets	95.78	98.89	99.20	99.52	99.92	99.96	99.84	**99.99**
Bare Soil	62.66	85.03	95.68	96.65	100.00	97.78	99.74	**100.00**
Bitumen	60.36	94.66	97.38	97.62	100.00	99.95	99.93	**100.00**
Bricks	81.19	92.51	85.97	97.16	98.10	94.84	98.75	**99.11**
Shadows	99.53	99.69	**100.00**	98.13	99.92	99.99	99.99	98.99
OA	84.24	94.43	92.44	96.76	98.07	96.28	98.96	**99.41**
AA	79.72	92.76	94.35	97.53	98.30	97.51	99.19	**99.29**
K	82.52	93.01	90.12	95.68	97.43	95.11	98.62	**99.21**

TABLE IV
CLASSIFICATION RESULTS ACHIEVED BY DEFERENT METHODS ON THE PAVIA CENTER IMAGE

Class	SVM	EMP	EMAP	EEP	ESP	SC-MK	SF-SP-SVM	SF-SP-MK
Dimensions	102	51	51	126	71	306	244	244
Water	99.65	99.87	**99.95**	99.67	99.36	99.68	99.45	99.64
Trees	90.38	**92.12**	90.61	89.74	88.04	91.95	90.61	91.05
Asphalt	91.65	90.02	91.10	91.57	94.08	**94.48**	92.38	92.01
Bricks	88.79	96.15	99.09	99.34	99.77	97.09	99.75	**99.78**
Bitumen	90.71	92.05	98.29	98.55	99.28	95.82	99.08	**99.32**
Tiles	94.89	96.76	96.53	97.40	**99.32**	95.28	98.69	98.76
Shadows	85.61	92.40	92.56	96.44	**99.02**	90.83	98.43	98.43
Meadows	96.73	98.39	98.92	98.91	97.72	98.33	98.93	**99.11**
Bare Soil	**99.98**	98.93	99.13	98.80	95.06	99.70	98.64	98.63
OA	96.60	97.85	98.31	98.41	98.38	97.87	98.58	**98.74**
AA	93.16	95.19	96.24	96.71	96.92	95.91	97.33	**97.41**
K	95.20	96.96	97.61	97.74	97.71	96.98	97.99	**98.22**

Table I presents the number of labeled samples for this image.

2) *University of Pavia:* The second HSIs were captured by the Reflective Optics System Imaging Spectrometer (ROSIS-03) sensor over the campus of the University of Pavia, Italy. This hyperspectral sensor captures the image in 115 bands with wavelengths from 430 to 860 nm. The geometric resolution of the ROSIS-03 sensor is 1.3 m per pixel. The size of this image is $610 \times 340 \times 103$, where 12 channels are discarded due to noise. Fig. 7 depicts the false-color image and the corresponding groundtruth map of this scene. Table I shows the number of samples about the reference classes.
3) *Pavia Center*: The third HSIs were also captured by the ROSIS-03 sensor. The image with 1096×489 pixels was taken over Pavia, northern Italy. Thirteen bands disturbed by noise have been deleted, resulting in a image with 102 channels. The color composite image of the Pavia Center dataset and the labeled samples are reported in Fig. 8. Table I shows the details about the reference classes.

B. Experimental Setting

To evaluate the effectiveness of the proposed approach, we compare it with several state-of-the-art HSIs classification methods, including the single kernel SVM [50], extended morphological profiles (EMP) [21], extended multiattribute profiles (EMAP) [51], extended extinction profiles (EEP) [52], the proposed extended saliency profiles (ESPs), superpixel-based

classification using multiple kernels (SC-MK) [53], and single kernel SVM using stacked spatial features extracted from superpixel of SP (SF-SP-SVM). The kernel adopted in single kernel SVM is RBF, which only considers the original spectral bands. EMP and EMAP model the spatial information by closing and opening with reconstruction and morphological attribute filters, respectively. For the EEP method, extinction profiles are constructed by repeatedly performing extinction filters on the first few principal components of the image. Extinction filter belongs to connected filters as the attribute filter, but it is extrema-oriented, which preserves the branches corresponding to the persistence of the extrema. In the ESP method, SPs extracted from different principal components are stacked and fed into the single kernel SVM classifier. SC-MK extracts the spatial features by the superpixel, and multikernel SVM is adopted to fuse the spatial features and spectral features. In SF-SP-SVM method, the spectral feature, SP^{mean}, and SP^{weight} are stacked and fed into the single kernel SVM.

In our experiments, the number of principal components for the Indian Pines, University of Pavia, and Pavia Center images is 25, 3, and 3, respectively. k_0 is set to 200, 5000, and 20000 for the tested Indian Pines, University of Pavia, and Pavia Center images, respectively. The parameter h_ν is fixed at 20 for the three tested data. To generate SP^{weight}, the parameter s is set to 500, and the σ is set to 1. In MKL, the weights of three base kernels μ^{spec}, μ^{mean}, and μ^{weight} are set to 0.2, 0.4, and 0.4, respectively, as reported in [53]. For the SVM method and other methods using single kernel SVM as the classifier, the optimized parameters of SVM are obtained by the fivefold cross-validation technique. For feature extraction, the parameters are set to the value referred to in the corresponding literature. For the EMAP method, two common attributes are used to build EMAP. Five thresholds for area attribute are [50, 100, 200, 500, 1000]. Eight thresholds of the standard deviation attribute are [10, 20, 30, 40, 50, 60, 70, 80]. For EMP, EEP, and SC-MK, the parameters are set as the recommended values reported in [21], [52], and [53], respectively. The dimensions of different features for the three datasets are reported in Tables II–IV, respectively.

For all tested datasets, the number of training samples is set to 50 per class, with the remaining samples used for testing. The classification accuracy is the average result of 10 experiments with different randomly selected training samples. The experiment results are compared quantitatively in terms of three evaluation metrics, including overall accuracy (OA), average accuracy (AA), and kappa coefficient (K). Additionally, the highest accuracies among the results given by different methods are showed as bold entities in Table II-VI.

C. Experiment Results

The classification maps of Indian Pines data obtained by different methods are shown in Fig. 9. It can be seen that, the classification performance of SVM is unsatisfactory owing to the salt-and-pepper noises. This phenomenon can be attributed to that SVM only utilizes spectral information, which ignores the spatial information inherited in the neighboring pixels of the image. The result of EMP is better than SVM, but the noise still occurred in the classification map. The classification maps of EMAP, EEP, ESP, SVM-CK, SC-MK, and SF-SP-SVM are superior to SVM, as the spatial context information of the image is utilized by these methods. As shown in Table II, the OA of ESP outperforms the EMP, EMAP, and EEP with 18%, 10%, and 9%, respectively. The saliency profile can extract spatial information of salient structures and strongly simplify the image, which preserves the homogeneity of objects. Specifically, SF-SP-MK shows the best result in terms of both quantitative and qualitative evaluation, followed by ESP and SF-SP-SVM. Moreover, the highest class-specific accuracies of the classes are all obtained by the proposed SF-SP-MK. The classification accuracy of SF-SP-SVM is slightly lower than ESP, which demonstrates that MKL can better mine the complementary information of different features.

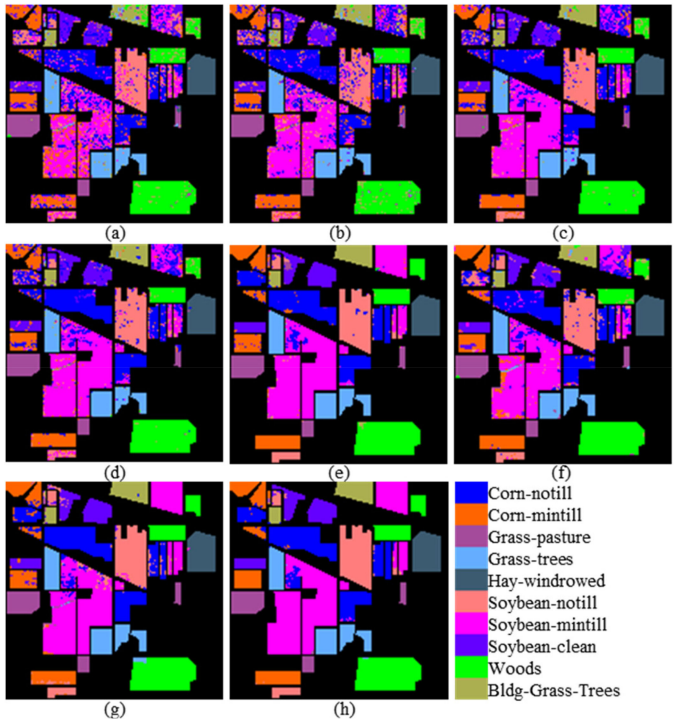

Fig. 9. Classification maps for the Indian Pines image. (a) SVM. (b) EMP. (c) EMAP. (d) EEP. (e) ESP. (f) SC-MK. (g) SF-SP-SVM. (h) SF-SP-MK.

The classification maps and accuracies given by different methods on the University of Pavia data are reported in Fig. 10 and Table III, respectively. Similar to the experiment results on the Indian Pines data, SF-SP-MK achieves the highest classification accuracy on the University of Pavia data. Specifically, ESP improves the classification accuracy of EMP, EMAP, EEP by approximately 3%, 5%, and 1%, respectively. By comparing the accuracies of SF-SP-SVM and SF-SP-MK methods, it can be proved that MKL can excavate the discriminative information hidden in different types of features. Specifically, the salt and pepper noises can be clearly seen in the classification maps of EMP, EMAP, EEP, and SC-MK, which are mainly occurred in the central bare soil area and the meadow area at the bottom. The proposed ESP and SF-SP-MK methods have significantly

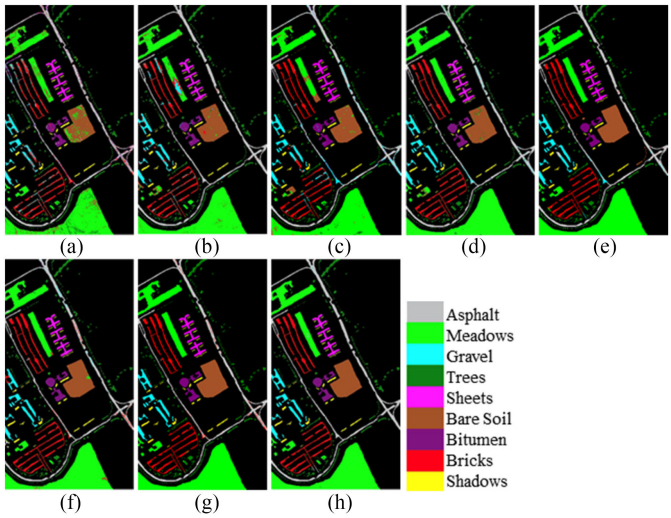

Fig. 10. Classification maps for the University of Pavia image. (a) SVM. (b) EMP. (c) EMAP. (d) EEP. (e) ESP. (f) SC-MK. (g) SF-SP-SVM. (h) SF-SP-MK.

improved the classification of these areas, since the irrelevant details are suppressed while selecting the salient shapes of ToS.

For the Pavia Center data, Table IV reports the classification results of different methods, and Fig. 11 shows the corresponding classification maps. Generally, the overall accuracies obtained by all methods broadly are all above 96%. The best accuracies are obtained by the SF-SP-MK, which demonstrates the effectiveness of the innersuperpixel and intersuperpixel features extracted from SP. Meanwhile, the SF-SP-MK achieves the highest average accuracy since it gives satisfactory results for all classes. In addition, the SF-SP-MK shows the improvement with spectrally similar classes, such as Self-Blocking Bricks and Bitumen.

Obviously, compared to the other morphological feature extraction method, SPs show better classification accuracy. It can be attributed to that, SPs can preserve salient shapes and reduce the complexity of the image by attenuating a lot of unimportant details, which significantly reduces the misclassification existed in the inside and border of the area for HSIs classification. Besides, innersuperpixel and intersuperpixel features extracted from morphological SPs are able to suppress the salt-and-pepper noise in the classification map. Furthermore, the SF-SP-MK outperforms the SF-SP-SVM for all datasets, which demonstrates that MKL provides a flexible framework to integrate the complementary information of spectral and spatial features.

D. Demonstration of Saliency Profiles Features

Fig. 12 shows the saliency profiles computed on the first three principal components of the University of Pavia data. It can be seen that, SP_i with smaller i keeps more detail of the input data, whereas SP_i with larger i considerably simplifies the image since it is closer to the root. Meanwhile, most of the shapes on the tree have been removed, while the salient structures are preserved. For instance, the original image has 53 653 shapes, but SP_0 only retains 2259 shapes. Besides, SPs are generated

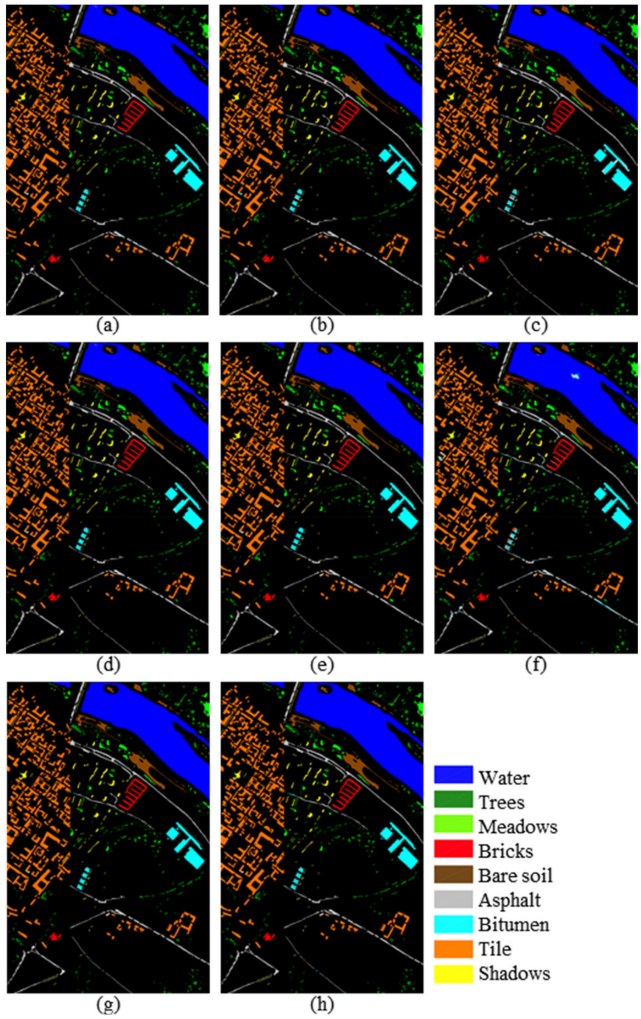

Fig. 11. Classification maps for the Pavia Center image. (a) SVM. (b) EMP. (c) EMAP. (d) EEP. (e) ESP. (f) SC-MK. (g) SF-SP-SVM. (h) SF-SP-MK.

by filtering the ToS layer by layer, and hence the structures that disappeared at the fine scale will not reappear at the coarse scale. The experiments illustrate that the SPs can capture salient structural information depending on the attribute function $\mathcal{A}_\nu$ and characterize specific size objects on feature maps at different scales. Besides, the dimensionality of SPs is only determined by the height of the tree $\mathcal{T}_0$, which means it is unrequired to set threshold values.

E. Effect of the Parameter h_ν and k_0

The classification result obtained with parameter h_ν ranging from 10 to 200 is shown in Fig. 13. It can be found that the classification results remain stable for the three tested data. For instance, the difference between the maximum OA and the minimum OA is less than 0.5% on three images, which demonstrates that the attribute function $\mathcal{A}_\nu$ are effective in selecting salient shapes whose edges coincide with the contours of land covers. The reason for this phenomenon is that, the attribute $\mathcal{A}_\nu$ of the salient node is always much larger than $\mathcal{A}_\nu$ of its parent node and child nodes. Therefore, the unimportant nodes

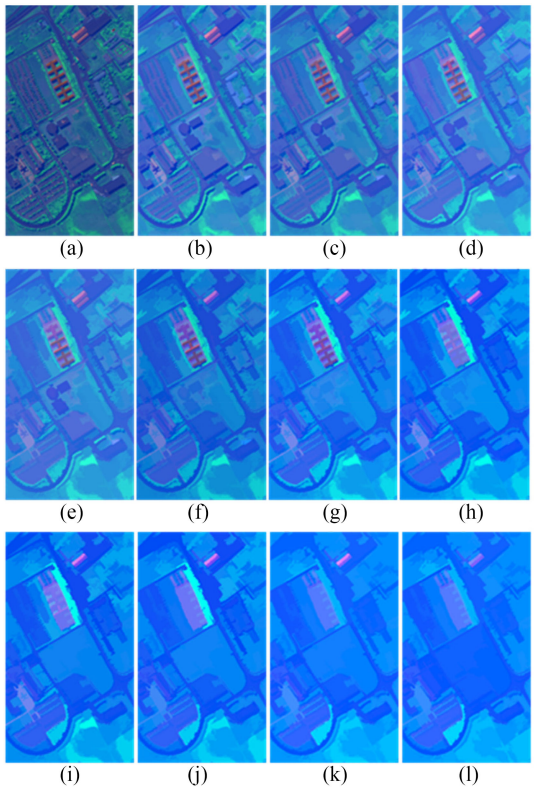

Fig. 12. SPs with different numbers of shapes computed on the University of Pavia image. (a) $PC_S(53653)$. (b) $PC_0(2259)$. (c) $PC_1(1072)$. (d) $PC_2(645)$. (e) $PC_3(416)$. (f) $PC_4(242)$. (g) $PC_5(170)$. (h) $PC_6(120)$. (i) $PC_7(103)$. (j) $PC_8(85)$. (k) $PC_9(60)$. (l) $PC_0(41)$.

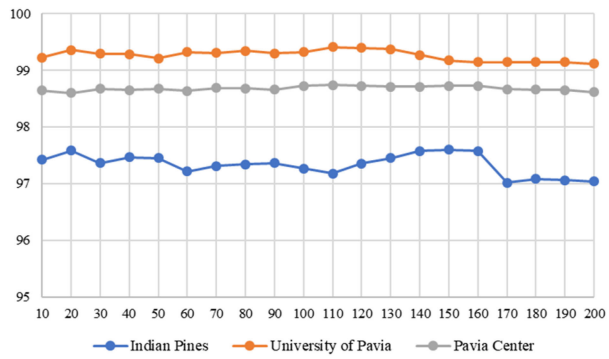

Fig. 13. Effects of parameter h_ν on different images.

including many insignificant maximum points on the curve of $\mathcal{A}_\nu$ can be removed, even with a small value of h_ν. Moreover, a larger h_ν can also retain the most important nodes while removing the unimportant notes. It can be observed from Fig. 13, the classification accuracy is insensitive to the parameters h_ν ranging from 10 to 200. Moreover, with the further increase of h_ν, more nodes on the ToS are removed, and abundant structural and detailed information will be ignored, which will lead to a decrease in the OA values. Thus, the parameter h_ν is set to be 20 for these three images.

The effects of k_0 on classification accuracy for the three datasets are shown in Fig. 14. Taking the spatial characteristics of the HSIs into consideration, the range of k_0 for the Indian

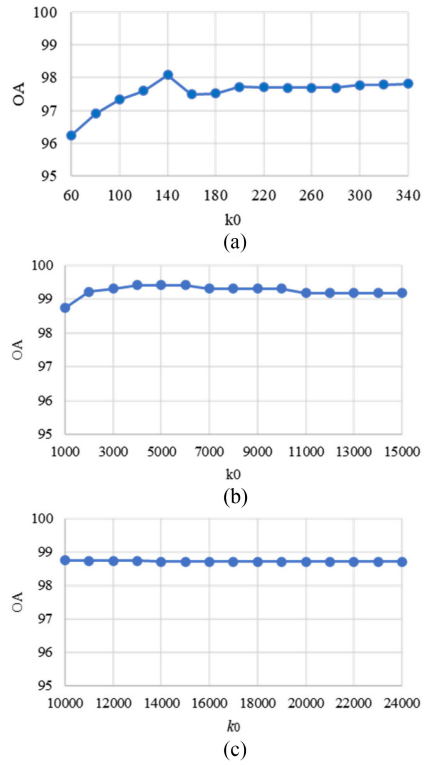

Fig. 14. Effects of parameter k_0 on different images. (a) Indian Pines image. (b) University of Pavia image. (c) Pavia Center image.

Pines data, the University of Pavia data, and the Pavia Center data varies from 60 to 340, 1000 to 15000, 10000 to 24000, respectively. The step size of k_0 for the Indian Pines data, the University of Pavia data, and the Pavia Center data is 20, 1000, and 1000, respectively. The curves represent the change of overall accuracy obtained by the proposed SF-SP-MK with different k_0. Specifically, for the University of Pavia, the proposed SF-SP-MK method shows satisfactory performances when the initial superpixel number varies from 4000 to 6000. The main reason for this phenomenon is that, the pixels that belong to different classes will be clustered into one superpixel when k_0 is set to a small value, which makes the information of different classes be introduced to the superpixel-based features. On the other hand, serious over-segmentation impedes the extraction of spatial features when k_0 is too large, which would also reduce the classification accuracy. It can be also noticed that, the variation of the overall accuracies is lower than 1% for the three HSIs. The main reason is that, the saliency profiles can attenuate the redundant details in the original image, and the objects in SPs images show more homogeneous characteristics. Thus, the spatial features that are derived from different superpixel segmentation results change little, leading to a stable classification curve.

F. Comparison of the Classifiers

To further test the performance of the proposed feature, three different classifiers including k-nearest neighbor (KNN), single kernel SVM, and random forest (RF) are taken into account. Table V shows the overall accuracy of classification obtained on

TABLE V
OVERALL ACCURACIES OBTAINED WITH DIFFERENT FEATURES AND CLASSIFIERS ON THREE DATASETS

Dataset	Indian Pines			University of Pavia			Pavia Center		
Classifier / Feature	KNN	SVM	RF	KNN	SVM	RF	KNN	SVM	RF
Spectral	60.89	72.41	69.53	70.14	84.24	73.31	94.95	96.6	94.67
EMP	55.98	74.20	83.79	82.06	94.43	90.62	96.86	97.85	97.69
EMAP	65.2	82.33	93.33	81.99	92.44	91.07	97.38	98.31	97.80
EEP	65.61	83.88	93.71	93.14	96.76	97.12	97.14	98.41	98.40
SC-MK	72.03	86.5	79.43	81.54	96.28	85.13	95.94	97.87	95.60
ESP	89.85	**95.00**	**95.96**	95.42	98.07	**98.30**	96.99	98.38	**98.45**
SF-SP	**91.26**	94.28	95.10	**96.20**	**98.96**	98.15	**97.41**	**98.58**	98.30

TABLE VI
CLASSIFICATION ACCURACIES GIVEN BY DIFFERENT APPROACHES ON THREE DATASETS

	Indian Pines			University of Pavia			Pavia Center		
Feature-Classifier	OA	AA	K	OA	AA	K	OA	AA	K
Spectral-SVM	72.41	77.97	68.38	84.24	79.72	82.52	96.60	93.16	95.20
SP-SVM	95.00	96.20	94.19	98.07	98.30	97.43	98.38	96.92	97.71
SF-SP-SVM	94.28	95.37	93.34	98.96	99.19	98.62	98.58	97.33	97.99
Spectral-KNN	60.89	65.43	55.33	70.14	79.48	62.50	94.95	90.53	92.89
SP-KNN	89.85	92.09	88.25	95.42	96.13	93.96	96.99	93.79	95.75
SF-SP-KNN	91.26	92.66	89.86	96.20	97.71	94.99	97.41	94.77	96.34
Spectral-RF	69.53	73.50	65.03	73.31	82.02	66.44	94.67	90.68	92.49
SP-RF	95.96	96.85	95.30	98.30	98.53	97.74	98.45	96.41	97.81
SF-SP-RF	95.10	96.03	94.30	98.15	98.40	97.54	98.30	96.89	97.60
SF-SP-MK	**97.72**	**98.28**	**97.34**	**99.41**	**99.29**	**99.21**	**98.74**	**97.41**	**98.22**

three datasets using KNN, SVM, and RF. Specifically, the K is set as 5 for the KNN classifier, and the number of trees for RF is set to 200. It can be observed from Table V that, both the proposed ESP and SF-SP achieve promising results. Specifically, for the KNN classifier, the highest accuracies are achieved with SF-SP on the three images. For the RF classifier, the best results are obtained with EPS, followed by SF-SP. Meanwhile, when using SVM as the classifier, the optimal result on the Indian Pines image is obtained with ESP, while the highest accuracy on the other dataset is obtained with SF-SP. The result proves that the proposed saliency profiles provide a better characterization for the spatial information of HSIs, which can improve the separability of different classes. Moreover, to validate the effectiveness of MKL in the proposed framework, the methods using different classifiers with different SP features are considered for comparison. As shown in Table VI, although the classification result given by ESP and SF-SP with the comparative classifiers are satisfactory, SF-SP-MK still achieves the best results on all of the datasets. It illustrates the superiority of the multikernel approach in fusing different kinds of features, which can better mine the complementary information of features.

IV. CONCLUSION

In this article, a hyperspectral image classification framework by exploiting the spectral–spatial information of SPs is proposed. Specifically, to mine the important object structures of the image, we propose a novel morphological feature, namely, saliency profiles, on the basis of the saliency index of the nodes on ToS. Then, a method that can adaptively determine the number of superpixels is developed and performed on each of the SPs to generate the superpixel segmentation maps. Subsequently, the innersuperpixel and intersuperpixel features are extracted by using the mean filter and weighted average filter. Finally, multiple kernel SVM is adopted to fuse the original spectral feature and innersuperpixel feature SP^{mean}, and intersuperpixel feature SP^{weight}.

The experiments conducted on three widely used hyperspectral data illustrate the superiority of the proposed method. The classification performances of the proposed method are better than the other state-of-the-art morphological methods, and the corresponding classification maps are more homogeneous in terms of visual interpretation. The reason is that, the attribute $\mathcal{A}_\nu$ measures the importance of shape based on its contour and contrast information, instead of the simple geometric metrics used in the traditional morphological features. Meanwhile, the experimental results obtained with different classifiers show that, the proposed features show better separating capability than the traditional morphological features, which benefit the recognition of objects in HSIs. Moreover, innersuperpixel and intersuperpixel features extracted from SPs are fused with spectral information by using MKL, which exploits the complementary information of different features and further improves the classification accuracy. In the future, we plan to combine the morphological features and deep learning approaches for hyperspectral image classification.

ACKNOWLEDGMENT

The authors would like to thank Prof. D. Landgrebe for providing the Hyperspectral data sets, and also the editors and the anonymous reviewers for their insightful and constructive comments, which helped to improve the article.

REFERENCES

[1] P. Ghamisi, J. Plaza, Y. Chen, J. Li, and A. J. Plaza, "Advanced spectral classifiers for hyperspectral images: A review," *IEEE Geosci. Remote Sens. Mag.*, vol. 5, no. 1, pp. 8–32, Mar. 2017.

[2] S. Asadzadeh and C. R. de Souza Filho, "A review on spectral processing methods for geological remote sensing," *Int. J. Appl. Earth Observ. Geoinformation*, vol. 47, pp. 69–90, 2016.

[3] M. Shimoni, R. Haelterman, and C. Perneel, "Hyperspectral imaging for military and security applications: Combining Myriad processing and sensing techniques," *IEEE Geosci. Remote Sens. Mag.*, vol. 7, no. 2, pp. 101–117, Jun. 2019.

[4] D. Haboudane, J. R. Miller, E. Pattey, P. J. Zarco-Tejada, and I. B. Strachan, "Hyperspectral vegetation indices and novel algorithms for predicting green LAI of crop canopies: Modeling and validation in the context of precision agriculture," *Remote Sens. Environ.*, vol. 90, no. 3, pp. 337–352, 2004.

[5] Q. Tong, Y. Xue, and L. Zhang, "Progress in hyperspectral remote sensing science and technology in China over the past three decades," *IEEE J. Sel. Topics Appl. Earth Observ. Remote Sens.*, vol. 7, no. 1, pp. 70–91, Jan. 2014.

[6] X. Shang and L. A. Chisholm, "Classification of Australian native forest species using hyperspectral remote sensing and machine-learning classification algorithms," *IEEE J. Sel. Topics Appl. Earth Observ. Remote Sens.*, vol. 7, no. 6, pp. 2481–2489, Jun. 2014.

[7] W. Song, W. Song, H. Gu, and F. Li, "Progress in the remote sensing monitoring of the ecological environment in mining areas," *Int. J. Environ. Res. Public Health*, vol. 17, no. 6, 2020, Art. no. 1846.

[8] P. Ghamisi *et al.*, "New frontiers in spectral-spatial hyperspectral image classification: The latest advances based on mathematical morphology, Markov random fields, segmentation, sparse representation, and deep learning," *IEEE Geosci. Remote Sens. Mag.*, vol. 6, no. 3, pp. 10–43, Sep. 2018.

[9] X. Jiang, Y. Zhang, Y. Li, S. Li, and Y. Zhang, "Hyperspectral image classification with transfer learning and Markov random fields," *IEEE Geosci. Remote Sens. Lett.*, vol. 17, no. 3, pp. 544–548, Mar. 2020.

[10] S. Jia, Z. Lin, B. Deng, J. Zhu, and Q. Li, "Cascade superpixel regularized gabor feature fusion for hyperspectral image classification," *IEEE Trans. Neural Netw. Learn. Syst.*, vol. 31, no. 5, pp. 1638–1652, May 2020.

[11] P. Duan, X. Kang, S. Li, P. Ghamisi, and J. A. Benediktsson, "Fusion of multiple edge-preserving operations for hyperspectral image classification," *IEEE Trans. Geosci. Remote Sens.*, vol. 57, no. 12, pp. 10336–10349, Dec. 2019.

[12] S. Yang, J. Hou, Y. Jia, S. Mei, and Q. Du, "Hyperspectral image classification via sparse representation with incremental dictionaries," *IEEE Geosci. Remote Sens. Lett.*, to be published, doi: 10.1109/LGRS.2019.2949721.

[13] F. Luo, L. Zhang, B. Du, and L. Zhang, "Dimensionality reduction with enhanced hybrid-graph discriminant learning for hyperspectral image classification," *IEEE Trans. Geosci. Remote Sens.*, to be published, doi: 10.1109/TGRS.2020.2963848.

[14] F. Luo, L. Zhang, X. Zhou, T. Guo, Y. Cheng, and T. Yin, "Sparse-adaptive hypergraph discriminant analysis for hyperspectral image classification," *IEEE Geosci. Remote Sens. Lett.*, vol. 17, no. 6, pp. 1082–1086, Jun. 2020.

[15] D. Hong, X. Wu, P. Ghamisi, J. Chanussot, N. Yokoya, and X. X. Zhu, "Invariant attribute profiles: A spatial-frequency joint feature extractor for hyperspectral image classification," *IEEE Trans. Geosci. Remote Sens.*, vol. 58, no. 6, pp. 3791–3808, Jun. 2020.

[16] P. Ghamisi, R. Souza, J. A. Benediktsson, X. X. Zhu, L. Rittner, and R. A. Lotufo, "Extinction profiles for the classification of remote sensing data," *IEEE Trans. Geosci. Remote Sens.*, vol. 54, no. 10, pp. 5631–5645, Oct. 2016.

[17] X. X. Zhu *et al.*, "Deep learning in remote sensing: A comprehensive review and list of resources," *IEEE Geosci. Remote Sens. Mag.*, vol. 5, no. 4, pp. 8–36, Dec. 2017.

[18] Z. Gong, P. Zhong, Y. Yu, W. Hu, and S. Li, "A CNN with multiscale convolution and diversified metric for hyperspectral image classification," *IEEE Trans. Geosci. Remote Sens.*, vol. 57, no. 6, pp. 3599–3618, Jun. 2019.

[19] Y. Chen, K. Zhu, L. Zhu, X. He, P. Ghamisi, and J. A. Benediktsson, "Automatic design of convolutional neural network for hyperspectral image classification," *IEEE Trans. Geosci. Remote Sens.*, vol. 57, no. 9, pp. 7048–7066, Sep. 2019.

[20] M. Pesaresi and J. A. Benediktsson, "A new approach for the morphological segmentation of high-resolution satellite imagery," *IEEE Trans. Geosci. Remote Sens.*, vol. 39, no. 2, pp. 309–320, Feb. 2001.

[21] J. A. Palmason, J. A. Benediktsson, and J. R. Sveinsson, "Classification of hyperspectral data from urban areas based on extended morphological profiles," *IEEE Trans. Geosci. Remote Sens.*, vol. 43, no. 3, pp. 480–491, Mar. 2005.

[22] S. Prasad and L. M. Bruce, "Limitations of principal components analysis for hyperspectral target recognition," *IEEE Trans. Geosci. Remote Sens.*, vol. 5, no. 4, pp. 625–629, Oct. 2008.

[23] F. Luo, H. Huang, Y. Duan, J. Liu, and Y. Liao, "Local geometric structure feature for dimensionality reduction of hyperspectral imagery," *Remote Sens.*, vol. 9, no. 8, 2017, Art. no. 790.

[24] F. Luo, B. Du, L. Zhang, L. Zhang, and D. Tao, "Feature learning using spatial-spectral hypergraph discriminant analysis for hyperspectral image," *IEEE Trans. Cybern.*, vol. 49, no. 7, pp. 2406–2419, Jul. 2019.

[25] M. Chini, N. Pierdicca, and W. J. Emery, "Exploiting SAR and VHR optical images to quantify damage caused by the 2003 Bam earthquake," *IEEE Trans. Geosci. Remote Sens.*, vol. 47, no. 1, pp. 145–152, Jan. 2009.

[26] J. Chanussot, J. A. Benediktsson, and M. Fauvel, "Classification of remote sensing images from urban areas using a fuzzy possibilistic model," *IEEE Geosci. Remote Sens. Lett.*, vol. 3, no. 1, pp. 40–44, Jan. 2006.

[27] H. G. Akçay and S. Aksoy, "Automatic detection of geospatial objects using multiple hierarchical segmentations," *IEEE Trans. Geosci. Remote Sens.*, vol. 46, no. 7, pp. 2097–2111, Jul. 2008.

[28] P. Ghamisi, M. S. Couceiro, J. A. Benediktsson, and N. M. F. Ferreira, "An efficient method for segmentation of images based on fractional calculus and natural selection," *Expert Syst. Appl.*, vol. 39, no. 16, pp. 12407–12417, 2012.

[29] P. Ghamisi, M. S. Couceiro, and J. A. Benediktsson, "Classification of hyperspectral images with binary fractional order Darwinian PSO and random forests," *Proc. SPIE*, vol. 8892, 2013, Art. no. 88920S.

[30] B. Luo and L. Zhang, "Robust autodual morphological profiles for the classification of high-resolution satellite images," *IEEE Trans. Geosci. Remote Sens.*, vol. 52, no. 2, pp. 1451–1462, Feb. 2014.

[31] M. Dalla Mura, J. A. Benediktsson, B. Waske, and L. Bruzzone, "Morphological attribute profiles for the analysis of very high-resolution images," *IEEE Trans. Geosci. Remote Sens.*, vol. 48, no. 10, pp. 3747–3762, Oct. 2010.

[32] P. Salembier and M. H. F. Wilkinson, "Connected operators: A review of region-based morphological image processing techniques," *IEEE Signal Process. Mag.*, vol. 26, no. 6, pp. 136–157, Jan. 2009.

[33] Y. Xu, T. Géraud, and L. Najman, "Connected filtering on tree-based shape-spaces," *IEEE Trans. Pattern Anal. Mach. Intell.*, vol. 38, no. 6, pp. 1126–1140, Jun. 2016.

[34] E. J. Breen and R. Jones, "Attribute openings, thinnings, and granulometries," *Comput. Vision Image Understanding*, vol. 64, no. 3, pp. 377–389, 1996.

[35] M. Dalla Mura, J. A. Benediktsson, B. Waske, and L. Bruzzone, "Extended profiles with morphological attribute filters for the analysis of hyperspectral data," *Int. J. Remote Sens.*, vol. 31, no. 22, pp. 5975–5991, 2010.

[36] P. Ghamisi, M. Dalla Mura, and J. A. Benediktsson, "A survey on spectral-spatial classification techniques based on attribute profiles," *IEEE Trans. Geosci. Remote Sens.*, vol. 53, no. 5, pp. 2335–2353, May 2015.

[37] R. Souza, L. Rittner, R. Machado, and R. Lotufo, "A comparison between extinction filters and attribute filters," in *Mathematical Morphology and Its Applications to Signal and Image Processing (Lecture Notes in Computer Science)*, Cham, Switzerland: Springer, 2015, vol. 9082, pp. 63–74.

[38] C. Vachier and F. Meyer, "Extinction value: A new measurement of persistence," in *Proc. IEEE Workshop Nonlinear Signal Image Process.*, 1995, vol. I, pp. 254–257.

[39] P. Ghamisi, B. Höfle, and X. X. Zhu, "Hyperspectral and LiDAR data fusion using extinction profiles and deep convolutional neural network," *IEEE J. Sel. Topics Appl. Earth Observ. Remote Sens.*, vol. 10, no. 6, pp. 3011–3024, Jun. 2017.

[40] B. Rasti, P. Ghamisi, J. Plaza, and A. Plaza, "Fusion of hyperspectral and LiDAR data using sparse and low-rank component analysis," *IEEE Trans. Geosci. Remote Sens.*, vol. 55, no. 11, pp. 6354–6365, 2017.

[41] Y. Xu, T. Géraud, and L. Najman, "Hierarchical image simplification and segmentation based on Mumford–Shah-salient level line selection," *Pattern Recognit. Lett.*, vol. 83, pp. 278–286, 2016.

[42] P. Monasse and F. Guichard, "Fast computation of contrast-invariant image representation," *IEEE Trans. Image Process.*, vol. 9, no. 5, pp. 860–872, May 2000.

[43] C. Ballester, V. Caselles, L. Igual, and L. Garrido, "Level lines selection with variational models for segmentation and encoding," *J. Math. Imag. Vision*, vol. 27, no. 1, pp. 5–27, 2007.

[44] D. Mumford, J. Shah, Z. Szallasi, J. Stelling, and V. Periwal, "Optimal approximations by piecewise smooth functions and associated variational problems," *Commun. Pure Appl. Math.*, vol. 42, no. 5, pp. 577–685, 1989.

[45] R. Achanta, A. Shaji, K. Smith, A. Lucchi, P. Fua, and S. Süsstrunk, "SLIC superpixels compared to state-of-the-art superpixel methods," *IEEE Trans. Pattern Anal. Mach. Intell.*, vol. 34, no. 11, pp. 2274–2281, Nov. 2012.

[46] T. Lu, S. Li, L. Fang, L. Bruzzone, and J. A. Benediktsson, "Set-to-set distance-based spectral-spatial classification of hyperspectral images," *IEEE Trans. Geosci. Remote Sens.*, vol. 54, no. 12, pp. 7122–7134, Dec. 2016.

[47] L. Fang, H. Zhuo, and S. Li, "Super-resolution of the hyperspectral image via superpixel-based sparse representation," *Neurocomputing*, vol. 273, pp. 171–177, 2018.
[48] X. Huang, Q. Lu, and L. Zhang, "A multi-index learning approach for classification of high-resolution remotely sensed images over urban areas," *ISPRS J. Photogramm. Remote Sens.*, vol. 90, pp. 36–48, 2014.
[49] D. Tuia, G. Camps-Valls, G. Matasci, and M. Kanevski, "Learning relevant image features with multiple-kernel classification," *IEEE Trans. Geosci. Remote Sens.*, vol. 48, no. 10, pp. 3780–3791, Oct. 2010.
[50] G. Mountrakis, J. Im, and C. Ogole, "Support vector machines in remote sensing: A review," *ISPRS J. Photogramm. Remote Sens.*, vol. 66, no. 3, pp. 247–259, 2011.
[51] P. R. Marpu, M. Pedergnana, M. D. Mura, S. Peeters, J. A. Benediktsson, and L. Bruzzone, "Classification of hyperspectral data using extended attribute profiles based on supervised and unsupervised feature extraction techniques," *Int. J. Image Data Fusion*, vol. 3, no. 3, pp. 269–298, 2012.
[52] P. Ghamisi, R. Souza, J. A. Benediktsson, L. Rittner, R. Lotufo, and X. X. Zhu, "Hyperspectral data classification using extended extinction profiles," *IEEE Geosci. Remote Sens. Lett.*, vol. 13, no. 11, pp. 1641–1645, Nov. 2016.
[53] L. Fang, S. Li, W. Duan, J. Ren, and J. A. Benediktsson, "Classification of hyperspectral images by exploiting spectral-spatial information of superpixel via multiple kernels," *IEEE Trans. Geosci. Remote Sens.*, vol. 53, no. 12, pp. 6663–6674, Dec. 2015.

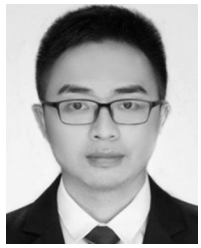

Qikai Lu (Member, IEEE) received the B.S. degree in remote sensing science and technology and the Ph.D. degree in photogrammetry and remote sensing from Wuhan University, Wuhan, China, in 2011 and 2016, respectively.

He is currently with the Faculty of Recourses and Environmental Science, Hubei University, Wuhan, China. His research interests include image processing, machine learning, and remote sensing applications.

Xuan Hu received the B.S. degree in surveying mapping engineering in 2016 from Wuhan University, Wuhan, China, where he is currently pursuing the M.S. degree in photogrammetry and remote sensing.

He is currently with the State Key Laboratory of Information Engineering in Surveying, Mapping, and Remote Sensing, Wuhan University, Wuhan, China. His research interests include image processing and remote sensing applications.